Oxygen vacancy induced structural evolution of $SrFeO_{3-x}$ epitaxial thin film from brownmillerite to perovskite

Seulki Roh, Seokbae Lee, Myounghoon Lee, Yu-Seong Seo, Amit Khare, Taesup Yoo, Sungmin Woo, Woo Seok Choi, and Jungseek Hwang*
Department of Physics, Sungkyunkwan University, Suwon, Gyeonggi-do 16419, Republic of Korea

A. Glamazda and K.-Y. Choi
Department of Physics, Chung-Ang University, Seoul 06980, Republic of Korea

(Received 28 September 2017; revised manuscript received 4 December 2017; published 2 February 2018)

We investigated $SrFeO_{3-x}$ thin films on a $SrTiO_3$ (001) substrate prepared via pulsed laser epitaxy using an optical spectroscopy technique. The oxygen vacancy level (x) was controlled by post-annealing processes at different oxygen partial pressures. We achieved a brownmillerite (BM) structure at $x = 0.5$ and observed the evolution of the crystal structure from BM into perovskite (PV) as the oxygen concentration increased. We observed the evolution of infrared-active phonons with respect to the oxygen concentration, which was closely related to the structural evolution observed via x-ray diffraction. We identified the phonons using the shell-model calculation. Furthermore, we studied temperature-dependent behaviors of the phonon modes of three representative samples: PV and two BMs (BM_{oop} and BM_{ip}) with different orientations of the oxygen vacancy channel. In the BM_{oop} sample, we observed a phonon mode, which exhibited an unusual redshift with decreasing temperature; this behavior may have been due to the apical oxygen instability in the FeO_6 octahedron. Our results provide important information regarding the ionic conduction mechanism in $SrFeO_{3-x}$ material systems.

DOI: 10.1103/PhysRevB.97.075104

I. INTRODUCTION

The multivalent nature of the transition-metal oxides gives rise to different oxygen stoichiometries that result in various physical properties [1–5]. Brownmillerite (BM) is a particular oxygen-deficient perovskite (PV) oxide structure that consists of alternating stacked layers of tetrahedral and octahedral units, with oxygen vacancy channels (OVCs) aligned in the tetrahedral layer. The OVC plays a key role in ionic conduction and/or oxygen storage [2,6–9]. It has been reported that BM transition-metal oxides, including $SrCoO_{3-x}$ (SCO), exhibit a topotactic phase transition, manifesting their ability to absorb oxygen [3,10]. SCO can be stabilized in two different crystalline phases depending on the oxygen content x: BM with $x = 0.5$ and PV with $x = 0$. These two phases can be reversibly switched by gaining or losing oxygen. On the other hand, the ionic conduction in BM is highly anisotropic, showing high conductivity along the OVC direction [7]. Notably, a different crystal plane of the substrate is adopted to achieve a different orientation of the OVC of the BM films on the substrate because the orthorhombic BM structure has different lattice constants with respect to the crystal axis. By switching the orientation of the OVC in the BM structure, a higher ionic conductivity can be achieved along the OVC, which is tilted 45° with respect to the chain of the tetrahedral units [2]. Owing to these interesting unique properties of the BM structure, it can be applied to various electronic devices [8,11].

$SrFeO_{3-x}$ (SFO) also shows topotactic phase transitions between BM and PV phases, which can be achieved at relatively low temperatures because their Gibbs free energy difference is small (on the order of 100 meV) [4]. $SrFeO_3$ has a PV crystal structure and exhibits metallic behavior. $SrFeO_{2.5}$ has a BM crystal structure, comprising alternately stacked FeO_6 octahedral and FeO_4 tetrahedral layers. The stacking axis is the orthorhombic b axis and the OVCs are along the orthorhombic [101] direction within the tetrahedral layers [4,5,12,13] [refer to the middle and bottom panels of Fig. 1(b)]. Interestingly, when $SrFeO_{2.5}$ is deposited on a $SrTiO_3$ (STO) (001) substrate via pulsed laser epitaxy (PLE), one can prepare two different $SrFeO_{2.5}$ BM thin film samples depending on the orientation of the oxygen-deficient (FeO_4) tetrahedral layer (ODTL) with respect to the film surface: one BM has ODTLs parallel to the film surface, or "in-plane ODTLs" [BM_{ip}; refer to the middle panel of Fig. 1(b)], and the other BM has ODTLs perpendicular to the film, or "out-of-plane ODTLs" [BM_{oop}; refer to the bottom panel of Fig. 1(b)]. Because the BM_{ip} and BM_{oop} films on STO (001) substrates exhibit similar free energies [9], the two different BM phases of the films are sensitive to their surrounding conditions; the two phases can compete with each other as kinds of order parameters [9,14]. The existence of these two possible BM phases on a substrate surface provides an opportunity to study not only the phonons in the ab plane but also the phonons along the c axis of the orthorhombic BM structure.

In this study, we prepared a series of $SrFeO_{3-x}$ (SFO) epitaxial thin films on an STO (001) substrate using PLE and subsequent post-annealing processes. The crystal structure of the prepared $SrFeO_{3-x}$ thin film varies from BM ($x = 0.5$) to PV ($x = 0$) depending on the oxygen deficiency level (x).

*jungseek@skku.edu

 ©2018 American Physical Society

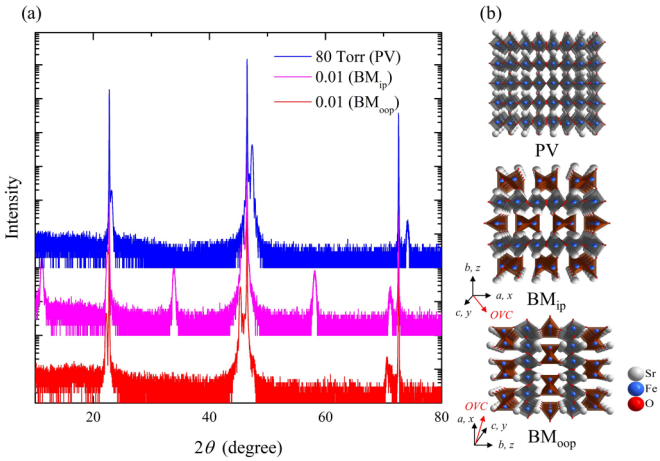

FIG. 1. (a) XRD data of three representative SFO films on STO (SFOs/STO) samples (some of the data are reproduced from Ref. [4]). (b) Three-dimensional crystal structures of the three crystal structures: PV and BM (BM_{ip} and BM_{oop}). x, y, and z axes also are marked for discussion in Sec. IV.

The oxygen deficiency level can be controlled according to the oxygen partial pressure (OPP) in the post-annealing processes. We performed an x-ray diffraction (XRD) experiment to investigate the evolution of the crystal structure. We used an optical spectroscopy technique to study the infrared-active (IR-active) phonon modes of the $SrFeO_{3-x}$ thin film samples. We observed the gradual evolution of the phonon modes as a function of the oxygen deficiency level. We also observed that the BM_{oop} sample exhibited quite different phonon modes from the BM_{ip} sample, as we measured different facets of the BM crystal. To identify and assign the optical phonon modes, we studied the Γ-point phonon modes by performing shell-model lattice dynamic calculations. We also cooled three (BM_{oop}, BM_{ip}, and PV) representative samples to examine the temperature-dependent properties of the observed phonon modes. We observed one interesting phonon mode in the BM_{oop} sample, which exhibited an unusual redshift with the temperature reduction. The unusual temperature-dependent behavior of this phonon mode is attributed to the instability of the apical oxygen in the octahedron [15].

II. SAMPLE PREPARATION

We prepared high-quality epitaxial $SrFeO_{3-x}$ thin film samples (≈18 nm thick) on a TiO_2-terminated STO substrate (001) using PLE at 700 °C. To obtain $SrFeO_{3-x}$ thin films, we treated the as-grown $SrFeO_{2.5}$ thin films in the BM_{oop} phase using a post-annealing process at 700 °C under different OPPs (0.01–500 Torr) for 10 minutes. Our as-grown $SrFeO_{2.5}$ sample shows the BM_{oop} phase, whose oxygen-deficient tetrahedral layers (ODTLs) are perpendicular to the film surface. However, 10 min of post-annealing under an OPP of 0.01 Torr at 700 °C changes the orientation to the BM_{ip} phase, whose ODTLs are parallel to the substrate surface. By adding oxygen to the prepared BM_{ip} $SrFeO_{2.5}$ thin film using a post-annealing process with various OPPs, we prepared a series of $SrFeO_{3-x}$ thin films, including the PV film. We denote our thin film samples according to their OPPs, which are 0.01, 0.05, 0.1, 0.5, 1, 80, and 500 Torr. Note that we have two different BM structures at the same OPP of 0.01: the as-grown structure (BM_{oop}) and the structure that was post-annealed (BM_{ip}) for 10 min. These two BM films have exactly the same crystal structure; the only difference is their orientations, which differ by 90°, as shown in Fig. 1(b).

Figure 1(a) shows XRD patterns of three representative SFO thin film samples. The lower two patterns show BM_{oop} (the lowest) and BM_{ip} (the middle). We can see the half-order peaks between the major peaks in the XRD pattern of the BM_{ip} sample. The existence of the half-order peaks indicates that the lattice constant parallel to the film surface is doubled by the 90° rotation of the orientation. As we increase the OPP further, the lattice constant ceases doubling along the film, and the crystal structure of the thin film transformed into a PV-like one, losing the half-order peaks in the XRD pattern. Figure 1(b) shows side views of three major crystal structures of our thin films: BM_{oop}, BM_{ip}, and PV. The horizontal substrate surface is located at the bottom of each crystal structure. Additional information regarding the sample preparation can be found in a previous work [4].

III. OPTICAL MEASUREMENT AND DATA ANALYSIS

Optical spectroscopy is an elegant experimental technique that can reveal the electronic and phononic structures of material systems. Here, we are interested in phonon modes, which are collective excitations of the lattice vibrations and can carry information regarding the crystal structure. Optical phonons usually have characteristic energy scales of far-IR (FIR) and mid-IR (MIR). We obtained reflectance spectra of our SFO thin films on STO substrates in the FIR region (50–700 cm^{-1}) using an FTIR-type spectrometer (Vertex 80v, Bruker) equipped with a 4.2 K bolometer detector. An *in situ* Au-evaporation technique was applied to obtain accurate reflectance spectra [16]. For the temperature-dependent experiments, the samples were cooled below room temperature using a continuous (liquid N_2) flow cryostat. Figure 2 shows the measured reflectance spectra of all our SFO thin films on STO (SFO/STO samples) along with the bare STO substrate in the FIR region. Because our films are thin (∼18 nm) and transparent in the FIR region, except for the frequencies of characteristic phonon modes, the reflectance spectra of all the SFO/STO samples appear similar to the typical reflectance spectrum of STO. In the FIR range, STO has four IR-active phonon modes: 93 (Slater mode), 176 (Last mode), 436 (appears below 105 K with the tetragonal phase transition), and 548 cm^{-1} (Axe mode) [17–21]. We clearly observe the three phonon modes of the STO substrate in the measured reflectance spectra of all the SFO/STO samples; they appear as strong dips near 50, 175, and 480 cm^{-1} in the reflectance. We can also observe small dips at various frequencies, which are the phonon modes of the $SrFeO_{3-x}$ thin films.

To separate the phonon modes of the SFO thin films from the measured reflectance spectra of the SFO/STO samples, we exploit the high and flat reflectance of the STO substrate in the FIR range. The available regions are 100–430 cm^{-1} [$R(\omega) \approx 97\%$] and 550–700 cm^{-1} [$R(\omega) \approx 88\%$]. By dividing the reflectance of the SFO/STO sample by that of STO in the available regions, we can obtain an *effective* transmittance spectrum of the SFO thin film. In this situation, the light

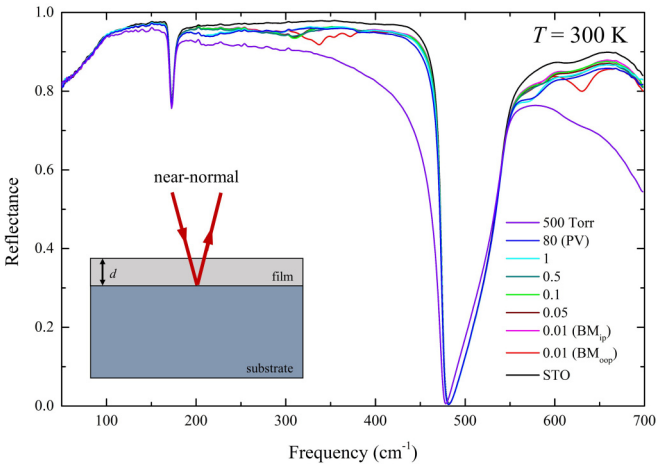

FIG. 2. Measured reflectance spectra of all the SFO/STO samples including the sample treated at OPP = 500 Torr and the bare STO substrate. Three strong phonon modes of the STO substrate are dominantly observable. The sample treated at OPP = 500 Torr exhibits a strong Drude absorption over the measured FIR range, while other samples show small dips caused by the phonon absorptions of the films.

from the source effectively passes through the SFO film twice before it arrives at the detector; it first goes though the SFO film, is then bounced back by the high-reflecting STO surface at the interface between the SFO and STO, and then passes through the SFO film a second time, as depicted in the inset of Fig. 2. We emphasize that this approach is reliable whenever the reflectance spectrum of the substrate is high and flat without any sharp features. Note that there are no absorptions by the insulating $SrFeO_{3-x}$ film in the FIR range, except for the absorptions by its phonons. However, as x decreases, the $SrFeO_{3-x}$ film becomes increasingly metallic. A metallic $SrFeO_{3-x}$ film exhibits an additional Drude absorption, as indicated by the reflectance spectrum of the SFO/STO sample treated at OPP = 500 Torr in Fig. 2. The strong Drude absorption governs the whole FIR spectrum and screens the phonon modes almost completely. Therefore, we exclude this SFO sample treated at 500 Torr from our subsequent discussion. We also tried to extract phonon modes using a multilayer model and found that our method described below is better to observe small intensity phonons (refer to the Supplemental Material (SM) [22]).

Having determined the *effective* transmittance spectra of the SFO thin films, we can go one step further to obtain the absorption coefficient spectra [$\alpha(\omega)$] of the SFO films using the well-known Beer's law, which can be written as follows:

$$\alpha(\omega) = -\frac{\ln T_{\text{eff}}(\omega)}{d_{\text{eff}}}, \tag{1}$$

where $T_{\text{eff}}(\omega)$ is the effective transmittance, and d_{eff} is the effective thickness of the SFO thin film, which is twice its physical thickness (d). After we obtain the absorption coefficient spectra of the SFO films, we fit the absorption coefficient spectra with a simple Lorentz model to find and identify the phonon modes. Here, we note that a Lorentz component corresponds to a phonon mode. The absorption coefficient can be expressed in terms of other optical constants, as follows:

$$\alpha(\omega) = \frac{4\pi\sigma_1(\omega)}{n(\omega)}, \tag{2}$$

where $\sigma_1(\omega)$ is the real part of the optical conductivity, and $n(\omega)$ is the index of refraction. The optical conductivity, which is given by $\tilde{\sigma}(\omega) \equiv \sigma_1(\omega) + i\sigma_2(\omega)$, can be written in the Lorentz model as follows:

$$\tilde{\sigma}(\omega) = \frac{i}{4\pi}\sum_j \frac{\Omega_{p,j}^2\,\omega}{\omega_{0j}^2 - \omega^2 + i\gamma_j\omega}, \tag{3}$$

where $\Omega_{p,j}$, ω_{0j}, and γ_j are the plasma frequency, the center frequency, and the width of the jth Lorentz (or phonon) component, respectively. The optical conductivity [$\tilde{\sigma}(\omega)$] is related to the complex index of refraction [$\tilde{N}(\omega) \equiv n(\omega) + i\kappa(\omega)$] as follows: $\tilde{N}(\omega) = \sqrt{i4\pi\tilde{\sigma}(\omega)/\omega + \epsilon_{\text{H}}}$, where $\kappa(\omega)$ is the extinction coefficient, and ϵ_{H} is the high-energy background dielectric constant. Because of the $n(\omega)$ in the denominator of Eq. (2), one additional oscillator centered at ω_0 may affect the absorption spectrum near ω_0; while it lowers the resulting $\alpha(\omega)$ below ω_0, it increases the resulting $\alpha(\omega)$ above ω_0. Therefore, individual modes may exceed the whole fit.

We calculated the Γ-point phonon modes to assign the symmetries to the observed IR-active phonon modes by performing shell-model lattice dynamical calculations using the General Utility Lattice Program (GULP) package [23]. The symmetry of the calculated modes was analyzed by the Bilbao Crystallographic Server [24]. In the shell model, the charge of the ion (Z) is treated as a combination of the sum of the point core with charge X and the massless shell with charge Y that models the valence electrons. The ionic polarizability $\alpha = Y^2/K$ can be described as a harmonic oscillator with a force constant K, which originates from the interaction between the core and the shell. The inter-ionic interactions can be represented as follows, including the long-range Coulomb potentials and short-range Born-Mayer-Buckingham potentials between ions i and j:

$$V_{\text{inter-ion}}(r) = A_{ij}\,e^{-(r/\rho_{ij})} - \frac{C_{ij}}{r^6}, \tag{4}$$

where A_{ij} and ρ_{ij} are the strength and range of the repulsive interaction, respectively, and C_{ij} is an attractive part with the inter-ionic distance r. The shell-model parameters are optimized by starting from well-documented data to achieve reasonable agreement with the experimental data [12,25].

IV. RESULTS AND DISCUSSION

The resulting shell-model parameters are summarized in Table I. For comparison, we also performed the shell-model lattice dynamical calculations for $SrFeO_3$. The adopted shell-

TABLE I. Adopted interatomic potential parameter for $SrFeO_{2.5}$.

Ions	Y (e)	K (eV/Å^2)	Atomic pair	A_{ij} (eV)	ρ_{ij} (Å)	C_{ij} (eV Å)
Fe^{3+}	1.0	990	Fe^{3+}-O^{2-}	3358.40	0.265	0
Sr^{2+}	1.0	30	Sr^{2+}-O^{2-}	3219.96	0.307	0
O^{2-}	−2.5	19	O^{2-}-O^{2-}	249.38	0.352	0

TABLE II. Resulting interatomic potential parameter for $SrFeO_3$.

Ions	Y (e)	K (eV/Å^2)	Atomic pair	A_{ij} (eV)	ρ_{ij} (Å)	C_{ij} (eV Å)
Fe^{3+}	1.029	915.4	Fe^{4+}-O^{2-}	1560.0	0.299	0
Sr^{2+}	1.831	9.5	Sr^{2+}-O^{2-}	1435.7	0.337	0
O^{2-}	−2.513	34.5	O^{2-}-O^{2-}	22764.0	0.149	0

model parameters are listed in Table II. The three T_{1u} modes are calculated at 172, 249, and 559 cm^{-1} (refer to the top panels of Fig. 3 and Fig. 4). The calculated modes agree reasonably well with the observed modes at 214, 294, and 578 cm^{-1}. The calculated eigenvectors of the three IR-active phonon modes are depicted in Fig. 4. To determine the crystal group of BM_{oop} and BM_{ip}, we performed dynamical calculations for the $Ibm2$, $Pbma$, and $Icmm$ crystal groups. We found that the $Pbma$ space group provides a better description of the experimental data with respect to the phonon energies and orientation dependence. Figure 3 plots the calculated IR-active phonon modes of the BM_{oop}, BM_{ip}, and PV crystal structures. Here, the BM_{oop} (BM_{ip}) probes the IR-active modes polarized in the yz (xy) plane. It is worthwhile to note that the x, y, and z axes correspond to the a, c, and b orthorhombic crystal axes, respectively [refer to Fig. 1(b)]. The displacement patterns of the representative normal modes are also plotted in Fig. 5.

Figure 6(a) shows the absorption coefficient spectra of all the SFO films, which were obtained from the effective transmittance spectra. The BM_{oop} sample exhibits distinct phonon features compared with the other samples, because we post-annealed the BM_{ip} under various OPPs. As the OPP increased, the phonon modes show a systematic evolution until OPP = 0.5 Torr, then an abrupt structural change in between OPP = 0.5 and 1 Torr, and then another systematic evolution up to OPP = 80 Torr and above. There might be

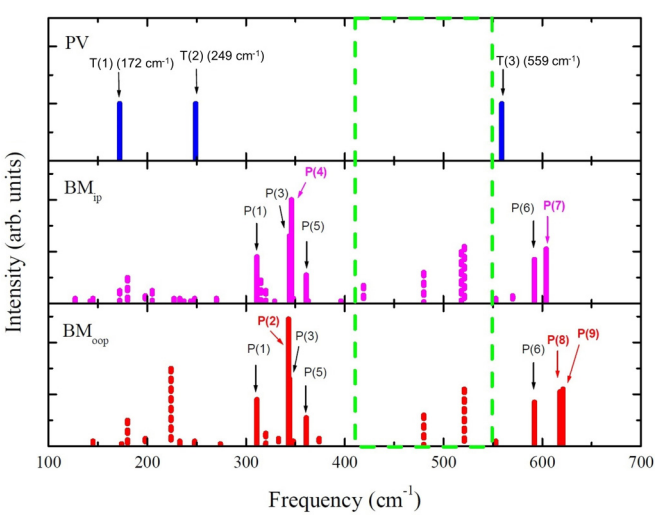

FIG. 3. Calculated IR-active modes of $SrFeO_3$ ($Pm\bar{3}m$) and $SrFeO_{2.5}$ ($Pbma$) for the BM_{ip} ($E\|x,y$) and BM_{oop} ($E\|y,z$) configurations. The intensity of the phonon peak is calculated using GULP, as described in the text. The phonons in the green dashed rectangle are not accessible with our experiment due to the strong phonons of the STO substrate.

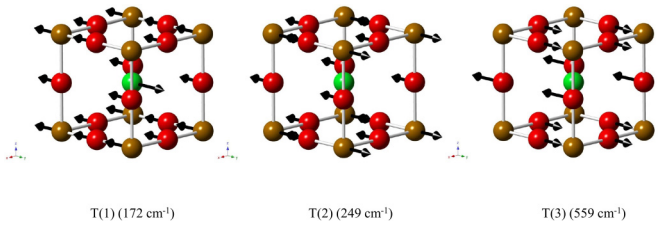

FIG. 4. Schematic representation of the calculated IR-active normal modes in $SrFeO_3$. The calculated frequencies are shown in parentheses. The amplitude of the vibrations is represented by the length of the arrows. The mustard-colored balls represent Fe, and the red and green balls represent oxygen and strontium atoms, respectively.

a structural crossover in between OPP = 0.5 and 1 Torr. We assigned selected nine phonon modes of BM structures, which are relatively strong and accessible with our experimental

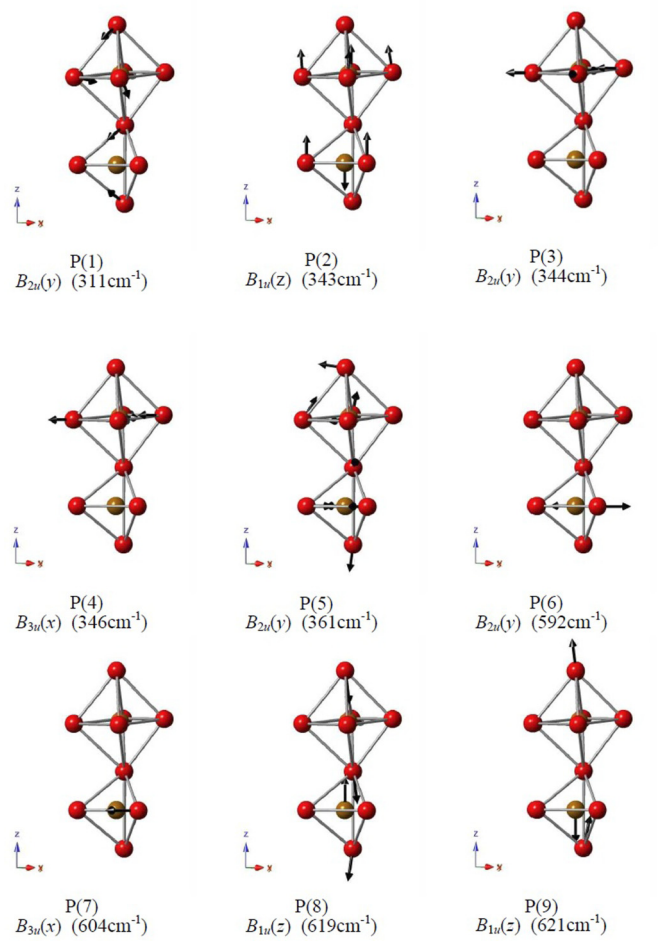

FIG. 5. Schematic representation of the most intensive IR-active modes P1–P9 with calculated frequencies in the parentheses. The related amplitude of the vibrations is represented by the arrow length. The mustard-colored balls represent Fe(1)/Fe(2) and Fe(3)/Fe(4) ions, which belong to the octahedron and tetrahedron, respectively. The red balls indicate the equatorial octahedron O(1)/O(2), tetrahedral O(5)/O(6), and apical O(3)/O(4). The modes including strontium vibrations are observed in the low-frequency region and have weak intensities. The strontium atoms are not shown, for clarity.

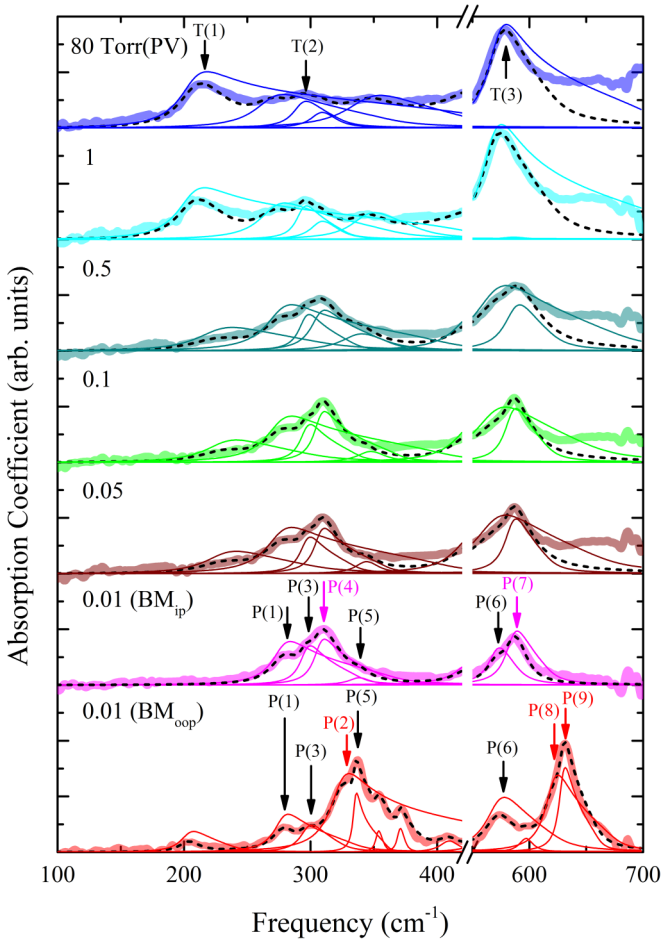

FIG. 6. Absorption coefficient spectra of all our SFO thin films at various oxygen vacancy levels. The thick lines represent measured data, and the thin lines represent separate phonon modes. The thick dashed black lines are the fits to the data. The phonons are assigned and labeled as P(1–9) for BM and T(1–3) for PV.

data, and labeled them as P(1–9) according to our shell-model calculations (refer to Fig. 3). The assigned modes are indicated with solid vertical lines in Fig. 3 and can be classified into two groups corresponding to Fe-O bending vibrations P(1, 3–5) and Fe-O stretching vibrations P(2, 6–9), which agree well with previous reports on other BM materials [26–28]. The three phonon modes of the PV phase are labeled as T(1–3).

The P(1) mode is observed in both the BM$_{oop}$ and BM$_{ip}$ absorption spectra. As the oxygen vacancy level decreases, this phonon mode softens, and its spectral weight is suppressed in the PV phases (OPP = 1 and 80 Torr). According to our calculation, the P(2) mode can be observed only in BM$_{oop}$ since it oscillates only along the z axis. We note that the assigned resonance frequency of the P(2) mode is relatively high compared with the assigned resonance frequencies of P(3) and P(4) (refer to Table III). The P(3) (344 cm^{-1}) can be seen in both BM$_{ip}$ and BM$_{oop}$ and has almost the same calculated resonance frequency as P(2) (343 cm^{-1}). P(3) exists even in the PV phase. The P(4) mode is observed only in the BM$_{ip}$, and as the OPP increases, the spectral weight of this phonon decreases significantly. The P(5) mode can be observed in the both BM$_{oop}$ and BM$_{ip}$ samples. We note that the P(5) mode of the Bm$_{oop}$ shows a stronger oscillation strength than that of the BM$_{ip}$ sample. According to the calculations the P(5) modes in both BM$_{oop}$ and BM$_{ip}$ vibrate along the y axis and their spectral weights are similar to each other as shown in Fig. 3. There are several shoulder peaks near this mode on the higher-frequency side in the BM$_{oop}$ sample. These shoulder peaks do not appear in the calculated phonon spectra and may come from the noncubic crystal symmetry of the BM$_{oop}$ sample [26–28]. P(6) is observed in both the BM$_{oop}$ and BM$_{ip}$ samples. As the oxygen vacancy level is reduced, this phonon mode becomes stronger, and when the BM sample is transformed into the PV structure, this phonon mode evolves to the T(3) mode. The P(7) phonon is only observed in the BM$_{ip}$ sample, and as the OPP increases, it loses its spectral weight and exhibits a slight redshift. When the structure transforms into the PV phase, the P(7) mode merges with the P(6) mode and evolves into the T(3) mode of the PV phase. The P(8) and P(9) modes are only observed in the BM$_{oop}$ and are related to the vibration of apical oxygen in the octahedron.

In the PV phase samples (1, 80 Torr), we observed not only the T(1–3) phonon modes but also three BM phonons [P(1, 3, and 4)], suggesting that the PV phase sample contained a majority of the PV phase and a minority of the BM$_{ip}$ phase. On the other hand, the 0.5 Torr sample shows the T(1) phonon, while its overall spectral shape is similar to BM$_{ip}$, which can be explained by the fact that this sample is a mixed phase with a majority of the BM$_{ip}$ phase. The mixed phase of the 0.5 Torr sample is consistent with previously reported XRD results [4]. Remarkably, according to a previous study [4], the SFO$_{3-x}$ thin film exhibits intermediate and homogeneous phases during the topotactic phase transition from BM to PV at

TABLE III. List of phonon symmetries and, experimental and calculated frequencies at the Γ point for SrFeO$_{2.5}$ with *Pbma* symmetry.

Mode	Expt. (cm^{-1})	Calc. (cm^{-1})	Assignment
P(1)	282	311	$B_{2u}(y)$ (FeO$_4$ and FeO$_6$ bending vibrations)
P(2)	**329**	343	$B_{1u}(z)$ (FeO$_4$ and FeO$_6$ stretching vibrations along the z axis)
P(3)	302	344	$B_{2u}(y)$ (FeO$_6$ and FeO$_6$ bending vibrations within the xy plane)
P(4)	311	346	$B_{3u}(x)$ (FeO$_6$ and FeO$_6$ bending vibrations within the xy plane)
P(5)	336	361	$B_{2u}(y)$ (FeO$_4$ and FeO$_6$ bending vibrations)
P(6)	577	592	$B_{2u}(y)$ (FeO$_4$ stretching vibration within the xy plane)
P(7)	589	604	$B_{3u}(x)$ (FeO$_4$ stretching vibration within the xy plane)
P(8)	**620**	619	$B_{1u}(z)$ (FeO$_4$ and FeO$_6$ stretching vibrations along the z axis)
P(9)	**629**	621	$B_{1u}(z)$ (FeO$_4$ and FeO$_6$ stretching vibrations along the z axis)

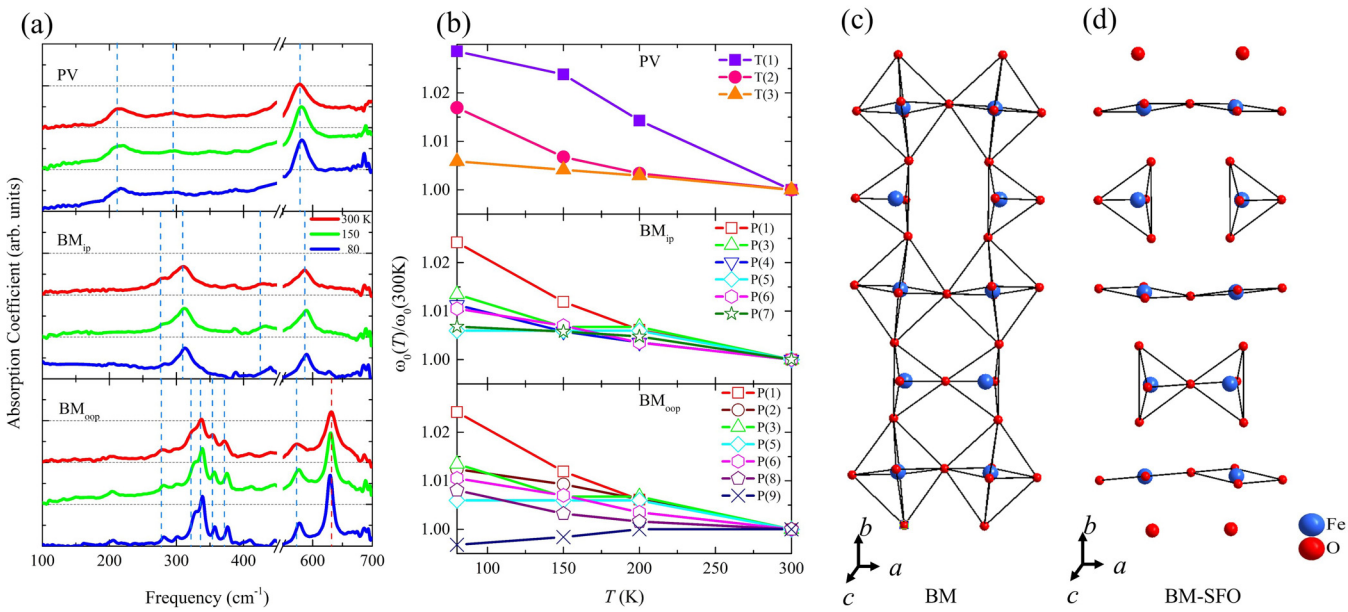

FIG. 7. (a) Temperature-dependent absorption coefficient spectra of three representative samples. The blue (blueshift) and red (redshift) vertical dashed lines are plotted to clearly illustrate the phonon shift. (b) Temperature-dependent $\omega_0(T)/\omega_0(300\text{ K})$ is displayed to illustrate the phonon shift. With cooling, the P(9) shows a redshift, while others exhibit blueshifts. (c) The normal BM crystal structure. The A atoms are not shown, for clarity. (d) BM crystal structure of SFO. The strontium atoms are not shown, for clarity. Here we drew (c) and (d) by referring to Fig. 7(a) and 7(b) of Ref. [15].

elevated temperatures owing to the itinerant oxygen. However, at room temperature, the film is stabilized as a mixed phase of BM and PV. Our phonon spectra show the same trends, providing more detailed structural information about our SFO thin films compared with the electronic structure analyses [10,29,30]. We note that P(2), P(8), and P(9) are observed only in the BM_{oop} sample since the oscillations involved are along only the z direction and their relative resonance frequencies are higher than those of other observed phonons compared with corresponding calculated resonance frequencies (refer to Table III). We speculate that these anomalous behaviors of the P(2), P(8), and P(9) modes are related to the apical oxygen instability.

Figure 7(a) shows the absorption spectra of our three representative samples in the BM_{ip}, BM_{oop} (OPP = 0.01 Torr), and PV (OPP = 80 Torr) phases at three selected temperatures. As the temperature decreases, the phonon modes become sharper, as the thermal smearing effects are reduced. At low temperatures, the lattice anharmonicity causes thermal contraction of the lattice, leading to a blueshift of the phonon frequencies. We included the vertical dashed lines to illustrate the temperature-dependent frequency shifts. We observe that all the phonon modes of interest are blueshifted (marked with the blue dashed lines), except for the phonon P(9) mode at $\sim$629 cm^{-1} in the BM_{oop} sample, which is marked with a red dashed line. To depict the phonon mode shift more clearly, we display the $\omega_0(T)/\omega_0(300\text{ K})$ of all the assigned phonons in Fig. 7(b), where $\omega_0(T)$ represents the center frequency of each phonon at the temperature, T. Only the P(9) mode exhibits a redshift by 0.3%; the other phonons undergo a blueshift by 0.6%–3.0%. This anomalous redshift is related to the instability of the apical oxygen in the BM_{ip} structure [20,31,32].

It has been reported that in the BM structure of $SrFeO_{2.5}$, the tetrahedral ordering may distort the octahedra, resulting in the instability of the apical oxygen of the octahedra. This instability causes the apical oxygens to be displaced away from the central Fe ion in the FeO_6 octahedron and towards the FeO_4 tetrahedron [6,15,33–35]. Because of these displacements, the typical alternating tetrahedral and octahedral layers are relaxed into a structure resembling that of $SrFeO_2$ with infinite $(FeO_2)_\infty$ layers and tetrahedral units between the layers as shown in Figs. 7(c) and 7(d). In this situation, the apical oxygens may experience two different bonding force fields along the symmetric axis of the octahedron: one is from the Fe ion in the FeO_4 tetrahedron unit, and the other from the Fe ion in the $(FeO_2)_\infty$ layers. We note that we did not clearly observe an additional phonon mode, which may be caused by the two different bonding force fields. The apical oxygen instability can cause the displacement of the apical oxygen from its original position in the octahedral FeO_6 and increases the bonding length between the apical oxygen and the Fe ion. Because of the greater bonding length, the bonding strength between the apical oxygen and the iron ion in the octahedron is significantly reduced. This bonding strength reduction may result in a stronger effect on the frequency of the related phonon [P(9)] than the unit cell volume contraction upon cooling, which may allow us to explain the observed abnormal redshift. This is our speculation; it is not possible to visualize the detailed structural changes with the temperature based on optical spectra alone.

Inoue *et al.* [7] reported that in BM, there are two oxygen diffusion pathways, which are highly anisotropic: diffusion within each tetrahedral or octahedral layer and diffusion through the tetrahedral and octahedral layer. Between theses, the diffusion within the layers is higher. This is supported

by our experimental results; i.e., the apical oxygen in the octahedron is instable, and the bonding force with the Fe is smaller than the equatorial one. Thus, the apical oxygen in the octahedron is more likely to participate in the ionic conduction. Moreover, the instability inherent to the BM SFO appears to trigger the low temperature oxygen mobility, which has been suggested by Paulus *et al.* [15].

V. CONCLUSION

We prepared $SrFeO_{2.5}$ epitaxial thin film samples (BM_{oop} and BM_{ip}) on an STO substrate using PLE. By treating the BM_{oop} samples with a post-annealing process at different OPPs, a series of SFO_{3-x} thin films were obtained. From measured reflectance spectra in the FIR region, we extracted the absorption coefficient spectra of all our samples. In the absorption coefficient spectra, we observed characteristic phonon modes of each sample and compared them with the results of shell-model calculations. We found that a sample treated at OPP = 0.5 Torr was an inhomogeneous mixed phase of BM_{ip} and PV phases with BM_{ip} phase dominance at room temperature, whereas samples treated at OPP = 1 and 80 Torr were a mixed phase with PV phase dominance at room temperature. We also found that the P(9) phonon mode is related to the Fe-O stretching and undergoes an abnormal redshift with cooling. We attribute this redshift to the instability of the apical oxygen in the octahedron. It is not yet completely understood how the apical oxygen instability is related to the ionic conduction mechanism. However, our results provide the important clue that the instability of the apical oxygens can trigger the ionic conduction, which was proposed by Paulus *et al.* [15]. This information enhances our understanding of the ionic conduction mechanism in these material systems. Furthermore, it provides better insight for designing the high ionic conducting materials.

ACKNOWLEDGMENTS

J.H. acknowledges financial support from the National Research Foundation of Korea (NRF-2017R1A2B4007387). This work was also supported by NRF-2017R1A2B4011083 (A.K. and W.S.C.).

[1] W. S. Choi, H. Jeen, J. H. Lee, S. S. A. Seo, V. R. Cooper, K. M. Rabe, and H. N. Lee, Phys. Rev. Lett. **111**, 097401 (2013).
[2] H. Jeen, Z. Bi, W. S. Choi, M. F. Chisholm, C. A. Bridges, M. P. Paranthaman, and H. N. Lee, Adv. Mater. **25**, 6459 (2013).
[3] H. Jeen, W. S. Choi, M. D. Biegalski, C. M. Folkman, I. C. Tung, D. D. Fong, J. W. Freeland, D. Shin, H. Ohta, M. F. Chisholm, and H. N. Lee, Nat. Mater. **12**, 1057 (2013).
[4] A. Khare, D. Shin, T. S. Yoo, M. Kim, T. D. Kang, J. Lee, S. Roh, I.-H. Jung, J. Hwang, S. W. Kim, T. W. Noh, H. Ohta, and W. S. Choi, Adv. Mater. **29**, 1606566 (2017).
[5] A. Khare, J. Lee, J. Park, G.-Y. Kim, S.-Y. Choi, T. Katase, S. Roh, T. S. Yoo, J. Hwang, H. Ohta, J. Son, and W. S. Choi, ACS Appl. Mater. Interfaces (2018), doi: 10.1021/acsami.7b17377.
[6] A. Piovano, M. Ceretti, M. R. Johnson, G. Agostini, W. Paulus, and C. Lamberti, J. Phys.: Condens. Matter **27**, 225403 (2015).
[7] S. Inoue, M. Kawai, N. Ichikawa, H. Kageyama, W. Paulus, and Y. Shimakawa, Nat. Chem. **2**, 213 (2010).
[8] J. E. Auckett, A. J. Studer, E. Pellegrini, J. Ollivier, M. R. Johnson, H. Schober, W. Miiller, and C. D. Ling, Chem. Mater. **25**, 3080 (2013).
[9] J. Young and J. M. Rondinelli, Phys. Rev. B **92**, 174111 (2015).
[10] H. Jeen, W. S. Choi, J. W. Freeland, H. Ohta, C. U. Jung, and H. N. Lee, Adv. Mater. **25**, 3651 (2013).
[11] S. K. Acharya, R. V. Nallagatla, O. Togibasa, B. W. Lee, C. Liu, C. U. Jung, B. H. Park, J.-Y. Park, Y. Cho, D.-W. Kim, J. Jo, D.-H. Kwon, M. Kim, C. S. Hwang, and S. C. Chae, ACS Appl. Mater. Interfaces **8**, 7902 (2016).
[12] C. Haavik, E. Bakken, T. Norby, S. Stolen, T. Atake, and T. Tojo, Dalton Trans. **2003**, 361 (2003).
[13] J. P. Hodges, S. Short, J. D. Jorgensen, X. Xiong, B. Dabrowski, S. M. Mini, and C. W. Kimball, J. Solid State Chem. **151**, 190 (2000).
[14] Y. Shimakawa, S. Inoue, M. Haruta, M. Kawai, K. Matsumoto, A. Sakaiguchi, N. Ichikawa, S. Isoda, and H. Kurata, Cryst. Growth Des. **10**, 4713 (2010).
[15] W. Paulus, H. Schober, S. Eibl, M. Johnson, T. Berthier, O. Hernandez, M. Ceretti, M. Plazanet, K. Conder, and C. Lamberti, J. Am. Chem. Soc. **130**, 16080 (2008).
[16] C. C. Homes, M. Reedyk, D. Cradles, and T. Timusk, Appl. Opt. **32**, 2976 (1993).
[17] J. Petzelt, T. Ostapchuk, I. Gregora, I. Rychetsky, S. Hoffmann-Eifert, A. V. Pronin, Y. Yuzyuk, B. P. Gorshunov, S. Kamba, V. Bovtun, J. Pokorny, M. Savinov, V. Porokhonskyy, D. Rafaja, P. Vanek, A. Almeida, M. R. Chaves, A. A. Volkov, M. Dressel, and R. Waser, Phys. Rev. B **64**, 184111 (2001).
[18] A. A. Sirenko, C. Bernhard, A. Golnik, A. M. Clark, J. H. Hao, W. D. Si, and X. X. Xi, Nature (London) **404**, 373 (2000).
[19] J. T. Last, Phys. Rev. **105**, 1740 (1957).
[20] P. A. Fleury, Annu. Rev. Mater. Sci. **6**, 157 (1976).
[21] I. Fedorov, V. Zelezny, J. Petzelt, V. Trepakov, M. Jelinek, V. Trtik, M. Cernansky, and V. Studnicka, Ferroelectrics **208**, 413 (1998).
[22] See Supplemental Material at http://link.aps.org/supplemental/10.1103/PhysRevB.97.075104 for details of a multilayer model fitting to obtain the phonon modes from the measured reflectance spectra.
[23] J. D. Gale, J. Chem. Soc., Faraday Trans. **93**, 629 (1997).
[24] M. I. Aroyo, A. Kirov, C. Capillas, J. M. Perez-Mato, and H. Wondratschek, Acta Crystallogr., Sect. A: Found. Adv. **62**, 115 (2006).
[25] V. Damljanovic, Ph.D. thesis, Max-Planck-Institut fur Festkorperforschung, Stuttgart, 2008.
[26] C. Tenailleau, A. Pring, S. M. Moussa, Y. Liu, R. L. Withers, S. Tarantino, M. Zhang, and M. A. Carpenter, J. Solid State Chem. **178**, 882 (2005).
[27] M. Karlsson, A. Matic, C. S. Knee, I. Ahmed, S. G. Eriksson, and L. Borjesson, Chem. Mater. **20**, 3480 (2008).
[28] J. Bielecki, S. F. Parker, D. Ekanayake, S. M. H. Rahman, L. Borjesson, and M. Karlsson, J. Mater. Chem. A **2**, 16915 (2014).
[29] E. Dagotto, Science **309**, 257 (2005).

[30] J. Mizusaki, M. Okayasu, S. Yamauchi, and K. Fueki, J. Solid State Chem. **99**, 166 (1992).
[31] R. P. S. M. Lobo, R. L. Moreira, D. Lebeugle, and D. Colson, Phys. Rev. B **76**, 172105 (2007).
[32] N. Nakanishi, A. Nagasawa, and Y. Murakami, J. Phys. Colloques **43**, C4 (1982).
[33] T. G. Parsons, H. D'Hondt, J. Hadermann, and M. A. Hayward, Chem. Mater. **21**, 5527 (2009).
[34] A. Glamazda, K. Y. Choi, P. Lemmens, W. S. Choi, H. Jeen, T. L. Meyer, and H. N. Lee, J. Appl. Phys. **118**, 085313 (2015).
[35] M. Haruta, H. Kurata, K. Matsumoto, S. Inoue, Y. Shimakawa, and S. Isoda, J. Appl. Phys. **110**, 033708 (2011).